RESEARCH ARTICLE | APRIL 04 2025

Enhanced MVA of polarized proton beams via PW laser-driven plasma bubble

Zhikun Zou ; Gan Guo ; Meng Wen ; Bin Liu ; Xue Yan ; Yangjié Liu ; Luling Jin

Matter Radiat. Extremes 10, 037202 (2025)
https://doi.org/10.1063/5.0249082

Matter and Radiation at Extremes

RESEARCH ARTICLE

pubs.aip.org/aip/mre

Enhanced MVA of polarized proton beams via PW laser-driven plasma bubble

Cite as: Matter Radiat. Extremes 10, 037202 (2025); doi: 10.1063/5.0249082
Submitted: 15 November 2024 • Accepted: 16 March 2025 •
Published Online: 4 April 2025

Zhikun Zou,[1] Gan Guo,[1] Meng Wen,[1,a)] Bin Liu,[2,b)] Xue Yan,[3] Yangjié Liu,[1] and Luling Jin[1,c)]

AFFILIATIONS

[1] Department of Physics, Hubei University, Wuhan 430062, China
[2] Guangdong Institute of Laser Plasma Accelerator Technology, Guangzhou, China
[3] School of Mechanical Engineering, Jiangsu University, Zhenjiang 212013, China

[a)] **Author to whom correspondence should be addressed:** wenmeng@hubu.edu.cn
[b)] **Electronic mail:** liubin@glapa.cn
[c)] **Electronic mail:** jinluling@hubu.edu.cn

ABSTRACT

The significance of laser-driven polarized beam acceleration has been increasingly recognized in recent years. We propose an efficient method for generating polarized proton beams from a pre-polarized hydrogen halide gas jet, utilizing magnetic vortex acceleration enhanced by a laser-driven plasma bubble. When a petawatt laser pulse passes through a pre-polarized gas jet, a bubble-like ultra-nonlinear plasma wave is formed. As a portion of the particles constituting this wave, background protons are swept by the acceleration field of the bubble and oscillate significantly along the laser propagation axis. Some of the pre-accelerated protons in the plasma wave are trapped by the acceleration field at the rear side of the target. This acceleration field is intensified by the transverse expansion of the laser-driven magnetic vortex, resulting in energetic polarized proton beams. The spin of energetic protons is determined by their precession within the electromagnetic field, which is described using the Thomas–Bargmann–Michel–Telegdi equation in analytical models and particle-in-cell simulations. Multidimensional simulations reveal that monoenergetic proton beams with an energy of hundreds of MeV, a beam charge of hundreds of pC, and a beam polarization of tens of percent can be produced at laser powers of several petawatts. Such laser-driven polarized proton beams have promise for application in polarized beam colliders, where they can be utilized to investigate particle interactions and to explore the properties of matter under extreme conditions.

I. INTRODUCTION

In recent years, high-powered laser facilities have become capable of delivering ultrashort pulses with an intense laser power surpassing 10 PW[1,2] and a pulse duration of less than 20 fs.[3,4] The development of PW lasers is geared toward fundamental applications, including fusion ignition systems and high-energy particle physics.[5,6] Benefiting from these intense laser facilities, highly energetic beams of electrons, ions, and photons can be produced through laser–plasma interactions.[7] Ion acceleration driven by ultra-intense lasers in plasmas has been intensively investigated through theoretical models and experimental studies over the past decades.[8,9] Several efficient acceleration mechanisms in laser–solid interactions have been experimentally demonstrated, such as target normal sheath acceleration (TNSA) and radiation pressure acceleration.[10–13] An experimental record of generating 150 MeV proton beams from a solid foil has been reported recently.[14,15] Furthermore, ion acceleration at high repetition rates naturally occurs in hydrodynamic flows with near-critical density,[16–18] where ions can be accelerated through various mechanisms such as bubble acceleration (BA),[19,20] shock acceleration (SA),[21,22] and magnetic vortex acceleration (MVA).[23–25]

Energetic polarized particle beams play a pivotal role in high-energy physics and nuclear physics. The collision of polarized particle beams provides a unique opportunity to study the spin structure of hadrons.[26–28] Polarized particle beams can be produced in traditional accelerators, but these are expensive and huge. For instance, the proton accelerators of the RHIC and JLEIC consist of an ion

linac injector with an energy of ~200 MeV and energy boosters with hundreds of GeV.[29–31] With the rapid development of PW laser facilities, compact and economical laser plasma accelerators have come to the rescue. Polarized particles can be generated by radiation polarization of a laser-accelerated beam[32–34] or by laser acceleration in a pre-polarized target.[35,36] Notably, laser-driven proton acceleration only works with the latter method because of the significantly larger mass-to-charge ratio of protons compared with electrons.[37,38] Recently, it has become possible for targets with polarized protons to be provided by dense polarized atomic hydrogen gas jets.[39,40] To date, studies of laser-driven polarized proton acceleration using these dense gas targets have primarily focused on feasibility verification, with demonstrations of 100 MeV polarized proton beams generated with PW lasers via the MVA scheme[38,41] or boosted SA.[42] The BA scheme has been demonstrated to be successful in producing GeV polarized proton beams with a 200 PW laser.[43] The production of such beams, however, becomes challenging with currently available laser power, owing to the existence of a self-injection threshold.[44,45] Current intense laser facilities provide PW pulses, while 100 PW lasers are still under construction.[1,2] Considering the requirements for polarized colliders,[26–28] it is worthwhile to pursue the goal of increasing the acceleration efficiency of polarized protons using a PW laser.

To enhance laser-driven ion acceleration in a gas jet, a variety of useful experimental techniques have been applied, including tight focusing of PW pulses near the diffraction limit[46,47] and high-density gas jet production with a hydrodynamic shock wave excited by a low-energy laser pulse.[48,49] Propagation of such intense pulses in dense hydrodynamic jets may excite bubble-like ultra-nonlinear plasma waves, where the intense oscillation of background ions becomes a part of the plasma wave. The condition of self-injection of the background ions in the plasma wave is relatively challenging for PW lasers. Nevertheless, the background ions in the plasma wave acquire significant energy, which could be expected to boost the further injection and acceleration in MVA at the rear side of the target.

In this paper, we demonstrate the generation of monoenergetic polarized proton beams with energies in the hundreds of MeV range from a PW laser in a pre-polarized hydrogen chloride gas jet within an enhanced MVA. When the intense laser pulse penetrates the target, atoms with pre-polarized nuclei are ionized and a nonlinear plasma wave is excited by a ponderomotive force. The motions of background electrons and ions induce strong electromagnetic fields in the laser plasma wave. These fields consist of the charge separation field and a vortex magnetic field, where the proton energy is enhanced and its spin precesses. Before the laser pulse leaves the target, protons are accelerated by the laser-driven plasma wave, in radial and forward directions, respectively. The dependence of proton precession on laser plasma parameters is analyzed. When the laser pulse leaves the target, the laser-driven magnetic vortex introduces a stationary electric field at the rear boundary. Protons from the density down ramp still oscillate longitudinally in the plasma wave, which may be trapped and further accelerated in the magnetic-vortex-enhanced stationary acceleration field. Our particle-in-cell (PIC) simulations indicate that monoenergetic polarized proton beams with energies of several hundred MeV can be generated using PW lasers.

II. SIMULATION SETUP

The driving laser is a tightly focused Gaussian pulse, with a focal radius $w_0 = 3\lambda$, a laser amplitude $a_0 = 120$, a pulse duration $T_L = 10\tau$, and linear polarization along the y axis, where $\tau = \lambda/c$ denotes the laser cycle and $\lambda = 800$ nm is the laser wavelength. The corresponding laser power $\mathcal{P}_L = (\pi^2/4)\mathcal{P}_0 a_0^2 w_0^2/\lambda^2$ attains 2.78 PW, where $\mathcal{P}_0 = 4\pi\varepsilon_0 m_e^2 c^5/e^2 \approx 8.7$ GW is the natural relativistic power unit, with ε_0 the vacuum permittivity, and m_e and $-e$ the electron mass and charge. A schematic illustrating the proton acceleration and spin depolarization in the laser-driven plasma field is presented in Fig. 1. A PW laser pulse irradiates an HCl gas target containing pre-polarized hydrogen atoms with relatively high density. The atoms are ionized rapidly, with the spin of their nuclei conserved. Such an ultra-intense PW pulse can penetrate into overdense plasma with density $n_e \lesssim a_0 n_c/2$,[50] where $n_c = \varepsilon_0 m_e \omega_L^2/e^2$ is the plasma critical density and ω_L is the laser frequency. A plasma channel is formed when the laser power exceeds $2\mathcal{P}_0$.[51,52] The channel radius depends on the laser power and the plasma density according to Refs. 24 and 53

$$\frac{R_{\rm ch}}{\lambda} \approx \left(\frac{a_0}{2\pi^2\sqrt{K}}\frac{w_0}{\lambda}\frac{n_c}{n_e}\right)^{1/3}. \tag{1}$$

Inside the plasma channel, the magnetic field produced by the laser-driven hot electrons and returned current depends linearly on the channel radius.[54] It is therefore estimated as

$$B_\varphi \approx \left(\frac{\pi a_0}{\sqrt{K}}\frac{w_0}{\lambda}\right)^{1/3}\left(\frac{n_e}{n_c}\right)^{2/3}\frac{m_e\omega_L}{e}. \tag{2}$$

This magnetic vortex field reaches 10^5 T, which results in significant proton spin precession.

Two-dimensional PIC simulations are performed using the EPOCH code, which has been extended to include spin effects.[55] We use a moving window of size $180\lambda \times 80\lambda$ represented by a grid of 3600×1600, with four pseudoparticles per cell for protons, one pseudoparticle per cell for chlorine nuclei, and four pseudoparticles per cell for electrons. Additionally, a time step according to the Courant–Friedrichs–Lewy condition with a Courant number

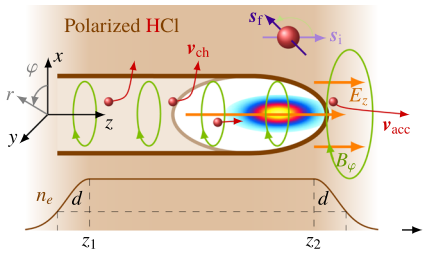

FIG. 1. Schematic showing the drive laser irradiating a gas jet of polarized HCl. A plasma channel is formed behind the laser bubble. Some background protons are pushed longitudinally by E_z, and protons with $\vec{v}_{\rm ch}$ are accelerated radially by the transverse field in the plasma channel. Meanwhile, the spin of protons precesses in the magnetic vortex according to Eq. (3). Transverse expansion of the magnetic vortex enhances the acceleration field at the rear boundary of the target. The forward-moving protons are trapped and accelerated to several hundred MeV.

of 0.95 is utilized in the simulations. The laser pulse is designed to focus onto the left boundary of the gas target at $z_1 = 50\lambda$. The target consists of a uniform plateau of $n_e = 0.54n_c$ in the region $z_1 \le z \le z_2$, and edges $n_e \exp\left[-(z-z_j)^2/d^2\right]$ on the up-ramp side $z < z_1$ and the down-ramp side $z > z_2$, where $j = 1, 2$, $d = 5\lambda$, and $z_2 = 250\lambda$. The corresponding densities of protons and chloride ions in the plasma are denoted by $n_p = n_{\mathrm{Cl}} = n_e/18$. The target thickness is the optimized laser depletion length $\sim a_0 T_L K n_c/n_e$.[56] The plasma target consists of electrons and nuclei derived by dissociation from pre-polarized HCl molecules,[40] with all protons initially polarized along the axis of laser propagation $\vec{s}_{\mathrm{i}} = \vec{e}_z$. The proton spin precession in the PIC code is described by the Thomas–Bargmann–Michel–Telegdi (TBMT) equation

$$\frac{d\vec{s}}{dt} = \frac{e}{m_p}\vec{s}\times\left[\left(G+\frac{1}{\gamma}\right)\vec{B} - \frac{G\gamma}{\gamma+1}\frac{\vec{v}\cdot\vec{B}}{c^2}\vec{v} - \left(G+\frac{1}{\gamma+1}\right)\frac{\vec{v}}{c^2}\times\vec{E}\right], \quad (3)$$

where $G \approx 1.79$ represents the anomalous magnetic moment of the proton, γ is the relativistic Lorentz factor, and m_p is the proton mass. In the nonrelativistic limit $v \ll c$, the precession frequency is determined by the first term of Eq. (3), which depends linearly on the magnetic field. In the magnetic vortex of the laser-driven plasma channel, we have

$$\Omega = (G+1)\frac{m_e}{m_p}\left(\frac{\pi a_0}{2\sqrt{K}}\frac{w_0}{\lambda}\right)^{1/3}\left(\frac{n_e}{n_c}\right)^{2/3}\omega_L. \quad (4)$$

III. PROTON DYNAMICS IN GAS JET

When an intense short laser pulse propagates through an underdense plasma, a laser-driven bubble is formed, with electrons being completely blown out by the ponderomotive force. Figure 2(a) shows an electron bubble with positive charges surrounding the drive laser within the plasma. The density of the positive charges is $\rho \approx n_{e0}e$. In the ultra-nonlinear scheme driven by a PW laser, the electron bubble is adjoined by a relativistic plasma channel with the same radius. In this adjoined bubble–channel structure, the electric field is strong enough to accelerate background ions.[19,57] The simulations are initialized as the intensity peak of the laser pulse reaches the position $z = 0$ at time $t = 0$. Figure 2(a) shows the charge density distribution at time $t = 250\tau$, when the laser front arrives at a position $z_{\mathrm{f}} \approx 245\lambda$. Electrons along the laser propagation axis are expelled forward to z_{f} and radially within the range $z_{\mathrm{f}} - cT_L \le z \le z_{\mathrm{f}}$, thereby forming the sheath of the front half of the bubble. Under the space charge effect, background electrons are drawn back toward the propagation axis, and they enclose the bubble at $z_{\mathrm{t}} \approx 220\lambda$. Furthermore, Eq. (1) gives the plasma channel radius $R_{\mathrm{ch}} \approx 4.76\lambda$ by taking the geometrical factor of 2D simulation as $K \approx 1/10$,[56] which coincides with the density boundary of the plasma channel behind the bubble in the region $z < z_{\mathrm{t}}$, as shown in Fig. 2(a). As well as the sheath of the bubble and the plasma channel, a filament composed of dense electrons and ions appears on the propagation axis at $x \approx 0$, owing to the motion of ions.[58,59] This filament exhibits distinct characteristics: inside the bubble, it mainly consists of trapped electrons, owing to the difference in charge–mass ratio between electrons and ions, revealed as a negative charge density; whereas behind the bubble, the positive charges are dominated by background

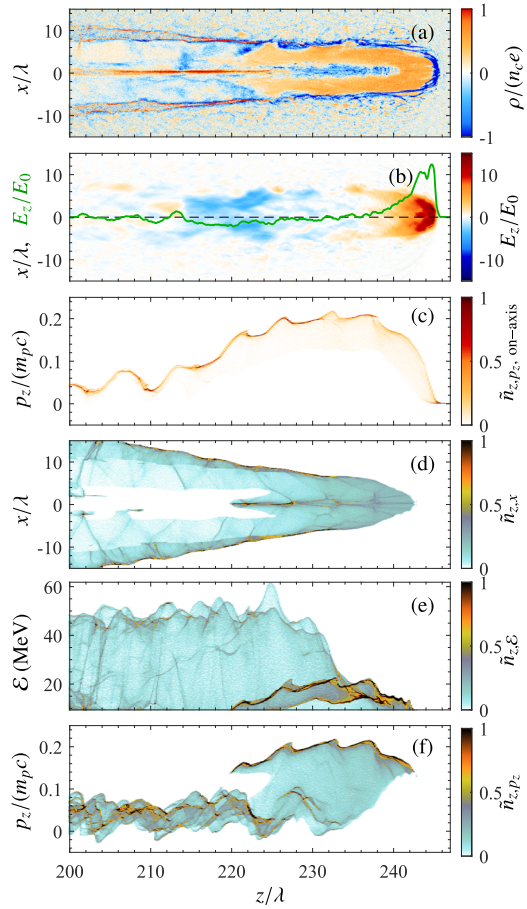

FIG. 2. (a) Snapshot in z–x space of the plasma charge density ρ (comprising the charge densities of electrons, protons, and chlorine nuclei) at $t = 250\tau$. (b) Snapshot in z–x space of the longitudinal electric field E_z at $t = 250\tau$. The solid green curve depicts the longitudinal electric field along the laser propagation axis at $x = y = 0$. (c) Density plot in z–p_z space of on-axis protons (with $|x| < 2\lambda$). (d)–(f) Density plots in z–x space, z–$\mathscr{E}$ space, and z–p_z space, respectively, of energetic protons (with energy larger than $\mathscr{E}_{\mathrm{min}} = 9.4$ MeV) at $t = 250\tau$.

ions that are pulled along the propagation axis by the electron filament.

The charge density distribution results in cylindrically symmetric charge separation fields E_z and E_{ch}, corresponding to the longitudinal electric field of the bubble and the radial electric field of the plasma channel, respectively. Figure 2(b) shows that the longitudinal component of the electric field in the plasma bubble has a large amplitude at the front of the bubble $z = z_{\mathrm{f}}$. The peak field strength is estimated as[60,61]

$$E_{z,\max} \approx \frac{\pi}{2^{1.5}}\left(1+\frac{v_{\mathrm{f}}}{c}\right)\sqrt{\frac{a_0 n_e}{n_c}}E_0, \quad (5)$$

with $v_{\mathrm{f}} = c/\sqrt{1+\pi^2 n_e/a_0}$ being the velocity of the dense electron layer at the front of the bubble and $E_0 = m\omega c/e$ the unit of electric

field. In addition to the charge separation and electric field, another characteristic of an ultra-nonlinear plasma wave is longitudinal motion of background protons.[44,45] The momenta of protons on the propagation axis with $r < 2\lambda$ are shown in Fig. 2(c), where the maximum momentum is found in the middle of the bubble. Taking account of Eq. (5), it is found that the protons oscillate in the plasma wave with maximum momentum[62]

$$p_{z,\max} = \frac{\pi^2}{16}\left(1 + \frac{c}{v_f}\right)^2 a_0 m_e v_f. \tag{6}$$

A density plot of energetic protons with energy $\mathscr{E} > 9.4$ MeV in z–x space is shown in Fig. 2(d). There are two groups of energetic protons, on and off the propagation axis, respectively. Density plots of these energetic protons at $t = 250\tau$ in z–$\mathscr{E}$ space and in z–p_z space are shown in Figs. 2(e) and 2(f), respectively. The on-axis group with $r < 2\lambda$ in Fig. 2(d) occupies the same region of the bubble $z_t < z < z_f$. These protons are pushed forward when the front half of the bubble passes by. Corresponding dense protons can be found within the bubble region of Figs. 2(e) and 2(f), with $\mathscr{E} \lesssim 20$ MeV and $p_z \gtrsim 0.15 m_p c$. The momentum given by Eq. (6) is about $0.16 m_p c$, which is qualitatively consistent with Figs. 2(c) and 2(f). Here, it should be noted that $v_{z,\max} \ll v_f$, with $v_{z,\max} = p_{z,\max}/(\gamma m_p c)$. This indicates that the on-axis group has not been trapped by the bubble, which is different from the self-injection case of BA.[43–45] The on-axis protons are accelerated in the bubble, acquiring forward velocity in the front half of the bubble, and decelerated in the rear half. In addition, the spin of the protons precesses in the plasma channel according to Eqs. (2) and (4), owing to the presence of the magnetic field. The magnetic vortex at $t = 250\tau$ is shown in Fig. 3(a). The distributions of energetic protons with respect to the longitudinal spin component s_z and transverse spin component s_x are shown in Figs. 3(b) and 3(c), respectively. The distribution of protons with respect to s_x is symmetric, since the proton spin precesses in the cylindrically symmetric magnetic vortex. Owing to the presence of the singularity of the magnetic vortex at $\sqrt{x^2 + y^2} = 0$, the spin precession of on-axis BA protons is restricted. Specifically, the spin distribution of the protons near the bubble front $z \to 240\lambda$ in Figs. 3(b) and 3(c), where $s_z \to 1$ and $s_x \to 0$, i.e., $\vec{s} \to \vec{s}_i$.

Notably, the radial acceleration of background protons in the bubble channel also seems to occur inside the gas jet. The off-axis group of protons with $x \gtrsim R_{ch}$ in Fig. 2(d) is mainly accelerated by the field E_{ch} and moves radially in the region $z \le (z_f + z_t)/2$. The corresponding energy shown in Fig. 2(e) is consistent with the proton energy accelerated by the strong electrostatic sheath field of the channel $\mathscr{E}_{ch} = a_0 mc^2$.[57,63] In other words, the SA protons are accelerated to a velocity $v_{ch} \approx \sqrt{2\mathscr{E}_{ch}/m_p}$ during a time duration $t_{ch} \approx 2R_{ch}/v_{ch}$. This time duration is determined by the laser intensity and plasma density as

$$t_{ch} = \frac{\lambda}{c}\left(\frac{2}{Ka_0}\right)^{1/6}\left(\frac{w_0}{\pi^2\lambda}\frac{n_c}{n_e}\right)^{1/3}\sqrt{\frac{m_p}{m_e}}. \tag{7}$$

Moreover, the proton spin precesses in the magnetic vortex field given by Eq. (2). This field is roughly $8E_0/c$ with the parameters that we have assumed and is comparable to the field shown in Fig. 3(a). Taking the precession frequency to be given by Eq. (4), the precession angle is then obtained as

$$\Theta = (G+1)(2a_0)^{1/6}\left(\frac{2w_0}{\lambda}\right)^{2/3}\left(\frac{\pi^2}{K}\frac{n_e}{n_c}\right)^{1/3}\sqrt{\frac{m_e}{m_p}}. \tag{8}$$

Since we are assuming a the PW laser and a near-critical dense gas jet, the precession angle of the SA protons Θ becomes roughly 2 rad. The corresponding longitudinal spin component $s_z = \cos\Theta$ approaches −0.43, in agreement with the minimum of s_z in Fig. 3(b).

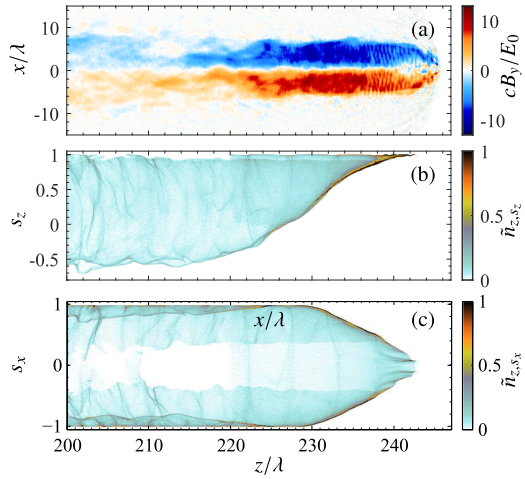

FIG. 3. (a) Snapshot in z–x space of the azimuthal magnetic field at $t = 250\lambda/c$. Here, the y component of the magnetic field B_y represents the azimuthal magnetic field B_φ in the plane $y = 0$. (b) and (c) Density plots in z–s_z space and z–s_x space, respectively, of energetic protons (with energy $\mathscr{E} > 9.4$ MeV) at $t = 250\lambda/c$.

IV. FIELDS IN THE REAR SIDE OF THE TARGET

When the drive pulse passes through the rear surface of the gas jet, a stationary acceleration field with magnitude given by Eq. (5) appears in the region behind the surface $z > z_2$. The charge density, acceleration field, and azimuthal magnetic field at $t = 270\tau$ are shown in Figs. 4(a)–4(c), respectively. It is found that the bubble shell expands transversely in the region $z > z_2$, which is accompanied by transverse expansion of E_z and B_φ. To show this expansion along the transverse direction, we set the horizontal axis of the plots in Fig. 4 along the x direction. It can be seen from Fig. 4(a) that half of the bubble leaves the flattop density of the gas jet at $t = 270\tau$. The bubble radius expands to 10λ at $z > z_2$, in comparison with the radius $R_{ch} \approx 5\lambda$ inside the gas jet at $z < z_2$. The acceleration field E_z in Fig. 4(b) has a static lower boundary at z_2, while its upper boundary moves with the laser-driven electron layer. It should be noted that the acceleration field is maintained at $E_z \gtrsim E_0$, as a result of electric field enhancement via the gradient of the magnetic vortex:

$$\partial_t E_z = c^2 \partial_r B_\varphi. \tag{9}$$

The increment in the electric field at $z = 270\lambda$ is plotted by the solid green curve in Fig. 4(d). It is consistent qualitatively with the

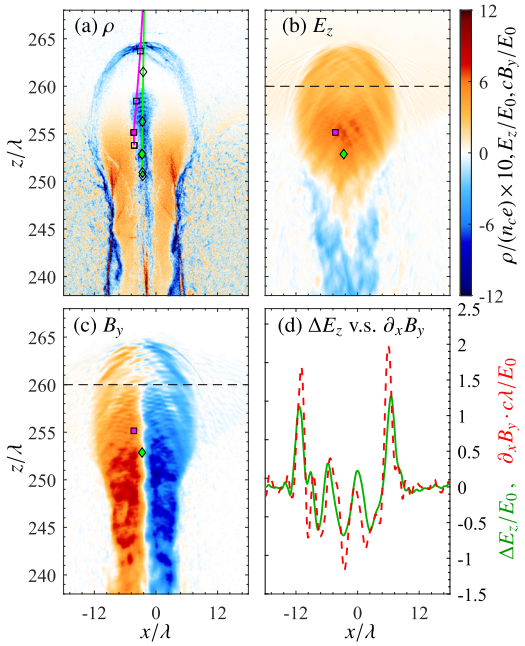

FIG. 4. (a)–(c) Snapshots in x–z space of the plasma charge density ρ, the longitudinal electric field E_z, and the azimuthal magnetic field B_y respectively, at $t = 270\tau$. The light green and magenta lines in (a) show the trajectories of two tracer protons, with diamond and square symbols indicating their positions along the respective trajectory. The solid green diamond and solid magenta square in (a)–(c) indicate the positions of each proton at $t = 270\tau$. (d) Comparison of the electric field increment in one laser cycle, $\Delta E_z = E_x|_{t=270.5\tau} - E_x|_{t=269.5\tau}$ (solid green curve), with the radial gradient of the azimuthal magnetic field, $\partial_r B_\varphi|_{y=0} = \partial_x B_y$ (dashed red curve), at $z = 270\lambda$.

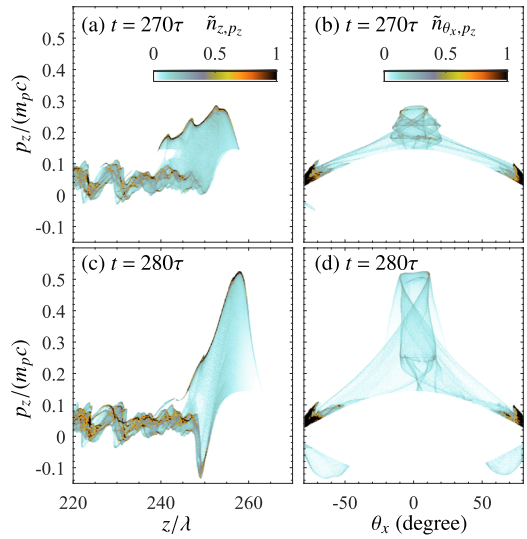

FIG. 5. (a) and (b) Density plots in z–p_z space and θ_x–p_z space, respectively, of energetic protons at $t = 270\tau$. (c) and (d) Corresponding density plots at $t = 280\tau$.

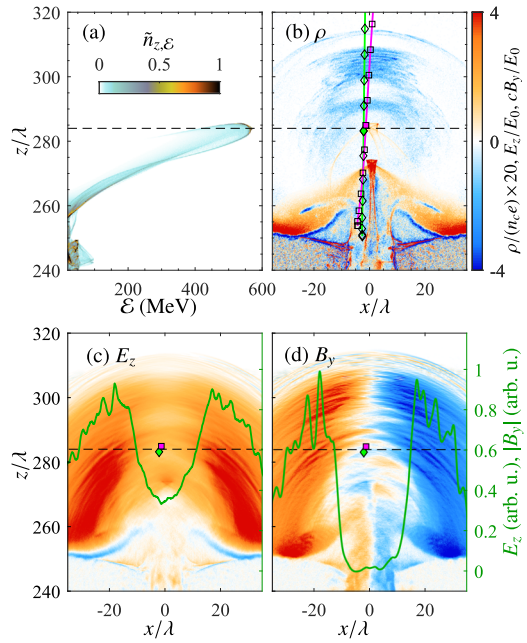

FIG. 6. (a) Snapshot of the phase-space distribution of energetic protons at $t = 320\tau$. (b)–(d) Snapshots in x–z space of the plasma charge density ρ, the longitudinal electric field E_z, and the azimuthal magnetic field B_y respectively, at $t = 320\tau$. The dashed black lines indicate the position $z = 284\lambda$ at which the maximum energy of protons appears. The corresponding longitudinal electric field and azimuthal magnetic field at $z = 284\lambda$ are shown by solid dark green curves in (c) and (d), respectively. As in Fig. 4, the light green and magenta lines and the diamond and square symbols in (b) show the trajectories of two tracer protons, with the solid diamond and square symbols in (b)–(d) indicating their positions at $t = 320\tau$.

radial gradient of the magnetic vortex field shown by the dashed red curve. Proton acceleration in this acceleration field enhanced by the stationary magnetic vortex is thus called MVA.[23] The axis of the magnetic vortex deviates slightly from the initial laser propagation axis, owing to hydrodynamic instability of the plasma.[64]

Energy enhancement of protons via MVA is the second stage of acceleration for the on-axis protons near the rear boundary of the target. They are accelerated first when they are swept by the acceleration field of the bubble, as described by Eqs. (5) and (6). The momentum distribution of the energetic protons along the propagation axis before they leave the gas target is shown at $t = 250\tau$ in Fig. 2(f). When the bubble passes the rear boundary at z_2, the pre-accelerated protons in the plasma wave are then trapped by the stationary field of MVA and accelerated to much higher energies. When the accelerated protons pass z_2, the longitudinal momentum component reaches $0.28 m_p c$ at $t = 270\tau$ and $0.52 m_p c$ at $t = 280\tau$, as depicted in Figs. 5(a) and 5(c), respectively. Figures 5(b) and 5(d) present the momentum distributions of energetic protons with respect to the spread angle $\theta_x = \tan^{-1}(p_x/p_z)$, from which it can be seen that only protons with small spread are accelerated forward. The accelerated beam comprises protons within a narrow spread angle, specifically, $\theta_x \lesssim 10^\circ$.

Figure 6(a) reveals that protons are accelerated to 550 MeV by $t = 320\tau$, with the maximum energy appearing at $z = 284\lambda$. These protons are found along the propagation axis with $|x| \lesssim \lambda$ in Fig. 6(b). The electron bunch in Fig. 6(b) around the energetic proton beam corresponds to the electron filament in Figs. 2(a) and 4(a). It also expands transversely into the region $x \lesssim 10\lambda$, where the magnetic vortex is evanescent. According Eq. (9), the on-axis acceleration field E_z is weakened when the negative radial gradient of the magnetic vortex moves radially from the propagation axis, as shown by the solid green curves in Figs. 6(c) and 6(d).

V. RESULTS AND DISCUSSION

When the energetic protons in the plasma wave are trapped by the magnetic vortex enhanced acceleration field, a monoenergetic proton beam can be produced. Energy spectra of protons from $t = 260\tau$ to 400τ are plotted by curves of different colors in Fig. 7(a). When the laser pulse propagates in the gas jet during $t \le 270\tau$, the cutoff energy is around 61 MeV, corresponding to the radially accelerated proton energy due to the plasma channel $\mathscr{E}_{ch}$. The cutoff energy is almost doubled to 116 MeV at $t = 280\tau$. Although the lower boundary of the MVA field in Figs. 4(b) and 6(c) stays at z_2, its amplitude decreases significantly when the negative radial gradient departs radially from the propagation axis, as illustrated in Figs. 6(c) and 6(d). As a consequence, only a portion of the protons in the plasma wave with higher longitudinal velocity component p_z, shown in Figs. 2(e) and 5(a), are trapped. As a result, energy peaks are found in the spectra at $t \ge 280\tau$ in Fig. 7(a). With the continuous acceleration of the trapped beam, the peak energy reaches 689 MeV at $t = 400\tau$. The production of the energy peak stems from the pre-acceleration of protons within the bubble, driven by a PW laser with an optimized plasma density. On the one hand, the effect of BA may diminish in plasmas with higher density, resulting in an energy spectrum of MVA protons that lacks a distinct energy peak.[23–25] On the other hand, self-focusing of the laser beam is weakened in plasmas with lower density, and the reduction of a_0 in Eqs. (5) and (6) decreases the acceleration of the protons.

The spin polarization of the accelerated proton beam is given by $P = |\langle \vec{s} \rangle|$, where $\langle\ \rangle$ indicates the average over all protons in the beam. In our setup, this polarization is roughly determined by $\langle s_z \rangle$ when the spin precession of beam protons occurs in the cylindrically symmetric magnetic vortex B_φ. The beam polarization is calculated on the basis of identifying beam protons, i.e., the protons in the accelerated beam. Since there is no energy peak in the spectra at $t < 280\tau$ in Fig. 7(a), beam protons cannot be identified with the energy spectrum when the laser pulse propagates in the gas jet. Alternatively, we identify the proton beam with protons in the peak of the longitudinal momentum spectrum, with $p_z > p_{z0}$. This is reasonable because, as shown in Fig. 5, both before and after the injection of MVA, the protons in the accelerated beam have relatively high p_z. A density plot of all energetic protons in p_z–s_z space at $t = 400\tau$ is shown in Fig. 7(b), where the longitudinal momentum spectra of all protons and the beam protons are shown by solid red and dashed black curves, respectively. The lower limit of the longitudinal momentum of the proton beam is given by $p_{z0} = 95\% p_{z,\mathrm{peak}}$, where $p_{z,\mathrm{peak}} = 1.42 m_p c$ corresponds to the peak value of the momentum

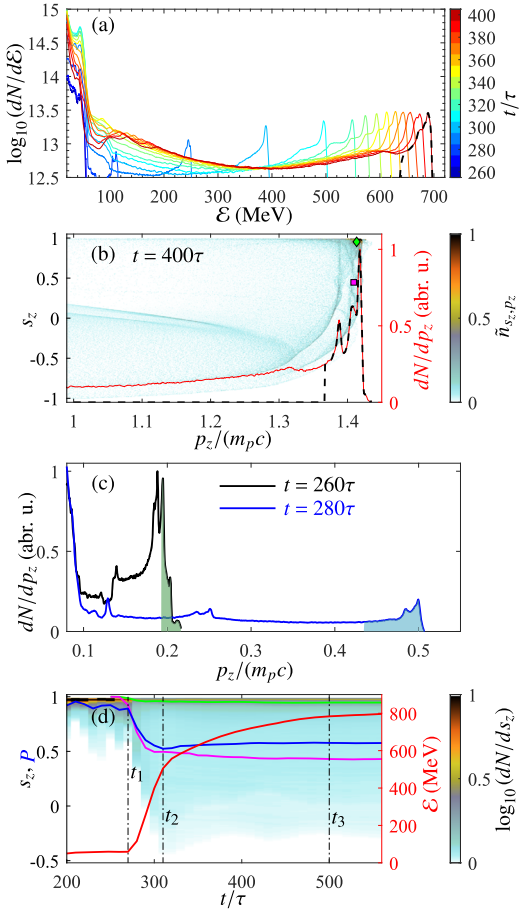

FIG. 7. (a) Energy spectra of protons at different times during $260\tau \le t \le 400\tau$. (b) Density plot in s_z–p_z space of protons at $t = 400\tau$, together with the longitudinal momentum spectra of all protons (solid red curve) and beam protons (dashed black curve). (c) Longitudinal momentum spectra at $t = 260\tau$ (black curve) and 280τ (blue curve). The shaded areas indicate the protons corresponding to those in the final accelerated beam. (d) Longitudinal spin spectrum of beam protons, dN/ds_z, as a function of time. The solid blue curve describes the dependence of the beam polarization $P = |\langle \vec{s} \rangle|$ on time. The cutoff energy of the accelerated protons is plotted by the solid red curve. The dashed black curve in (a) corresponds to the accelerated beam protons shown by the black dashed curve in (b). The magenta square and the green diamond in (b) indicated the locations of the two tracer particles, as in Fig. 4. The magenta and green curves in (d) show the variations of their respective values of s_z with time.

spectrum at $t = 400\tau$. The number of beam protons can be calculated from the momentum spectrum as

$$N_0 = \int_{p_{z0}}^{\infty} \frac{dN}{dp_z}\, dp_z. \tag{10}$$

Since the number of protons in the accelerated beam remains stable, one can consider protons with relatively high momentum, with the same number N_0, as representative of the beam protons throughout the entire acceleration process. In other words, at times $t \ne 400\tau$, the lower limit of momentum p_{z0} is determined by Eq. (10) with $N_0 = N_0|_{t=400\tau}$, rather than $p_{z,\mathrm{peak}}$. The beam protons at $t = 260\tau$ and

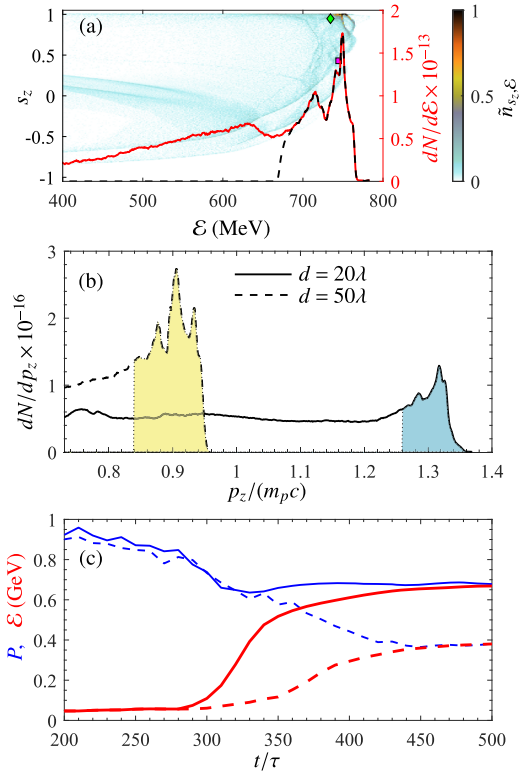

FIG. 8. (a) Density plot in $\mathscr{E}$–s_z space of protons at $t = 500\tau$, together with the energy spectra of all energetic protons (solid red curve) and the accelerated beam protons (dashed black curve). The magenta square and the green diamond indicate the locations of the two tracer particles, as in Fig. 4. (b) Longitudinal momentum spectra of accelerated protons at $t = 500\tau$ for density ramp lengths $d = 20\lambda$ (solid curve) and 50λ (dashed curve). (c) Evolution of maximum energy (red curves) and beam polarization (blue curves) over time for $d = 20\lambda$ (solid curves) and 50λ (dashed curves).

280τ are depicted by the shaded areas of the momentum spectra in Fig. 7(c). This reveals that only a small fraction of protons at the momentum peak at $t = 260\tau$, while still within the target, will be trapped into the final accelerated beam. The corresponding energy spectrum of the beam protons is plotted by a dashed black curve in Figs. 7(a) and 8(a). With the above definition of beam protons, protons of the same number N_0 with $p_z \geq p_{z0}$ are taken into account to calculate the beam polarization for the whole process of acceleration. The beam polarization $\langle s_z \rangle$ is thus obtained, with $P = 92\%$, 55%, and 57% at $t = 200\tau$, 300τ, and 400τ, respectively.

The time evolution of beam polarization is shown by the solid blue curve in Fig. 7(d), where the solid red curve represents the evolution of the cutoff energy of the accelerated proton beam. This reveals that the protons acquire energy $a_0mc^2/2$ before $t_1 = 270\tau$, when the laser pulse propagates in the plasma. As illustrated in Figs. 2(f) and 3(b), the proton beam consists of protons with relatively high longitudinal momentum. Therefore, the beam retains a relatively high polarization when the laser propagates inside the target. It can be seen from Fig. 7(d) that a strong energy increase and strong depolarization appear in the time interval $t_1 \leq t \leq t_2$, when the laser passes though the rear boundary of the target and energetic protons experience MVA. The MVA almost comes to an end when the energy reaches 495 MeV at $t_2 = 310\tau$. Subsequently, the acceleration field around the propagation axis becomes weaker, and the magnetic field almost vanishes, as seen in Figs. 6(c) and 6(d). The protons are accelerated slowly with the residual electron bunch until $t_3 = 500\tau$, and the proton beam polarization is sustained after t_2. A density plot of protons in $\mathscr{E}$–s_z space at $t = 500\tau$ is depicted in Fig. 8(a). The solid red curve and the dashed black curve represent the energy spectra of all protons and the beam protons, as defined by Eq. (10), respectively. The energy spectrum reveals an energy peak at 749 MeV, and the beam polarization is 66%.

To compare the spin dynamics of different protons in the accelerated beams, we trace two typical protons with the same longitudinal momentum $p_z = 1.41m_pc$ but different longitudinal spin components s_z at the momentum peak in Fig. 7(b). These are named as proton A and B, and their locations are indicated in all the relevant figures by a green diamond and magenta square, respectively. The corresponding evolutions of their s_z are plotted by green and magenta solid curves in Fig. 7(d), from which it can be seen that the longitudinal spin component of proton A remains above 94.5% for the whole process, while that of proton B falls below 50% when $t > t_2$. The different spin dynamics of protons A and B can be understood from their trajectories, which are plotted by green and magenta lines in Figs. 4(a) and 6(b). It is found that both of these originate from the down ramp of the gas jet, with $z_2 \lesssim z < z_2 + d$. More importantly, proton A originates from the propagation axis of the drive pulse and moves along it. By contrast, proton B originates from an off-axis location and moves forward with a diverging angle. When protons A and B are accelerated in almost the same electric fields, A remains along the propagation axis with zero magnetic field, while B experiences a stronger magnetic field beside the propagation axis, as shown by their locations in Figs. 4(a)–4(c) and 6(b)–6(d). The positions of protons A and B in $\mathscr{E}$–s_z space at $t = 500\tau$ are indicated in Fig. 8(a). One may conclude that protons with initially smaller deviation from the propagation axis contribute to the portion of protons with higher polarization in the accelerated beam.

Longitudinal momentum spectra of accelerated proton beams at $t = 500\tau$ from gas jets with density ramp lengths $d = 20\lambda$ and 50λ are shown in Fig. 8(b), where peaks can be seen at $p_z = 1.32m_pc$ and $0.91m_pc$, respectively. If the beam protons are defined by the same lower limit of proton momentum $p_{z0} = 95\%p_{z,\mathrm{peak}}$ in Fig. 8(b), one obtains beam polarizations of 67.8% and 38%, respectively. Figure 8(c) shows the corresponding evolution of the polarization of the accelerated beams and the cutoff energy for $d = 20\lambda$ and 50λ. Similar characteristics are found as for the case of $d = 5\lambda$ [Fig. 7(c)]: the proton beams are intensely accelerated and depolarized when the laser pulse propagates through the density down-ramp, with the corresponding time duration for beam acceleration and depolarization $t_2 - t_1$ depending linearly on d. The cutoff energies in Fig. 8(c) are 668 and 380 MeV for $d = 20\lambda$ and 50λ, respectively. It is found that the proton beam obtained with $d = 20\lambda$ has similar beam energy and polarization to the $d = 5\lambda$ case shown in Fig. 7. Therefore, a density scale length of the gas jet of the order of tens of micrometers is required within an experimentally realizable gas target with sharp gradient.[65–71]

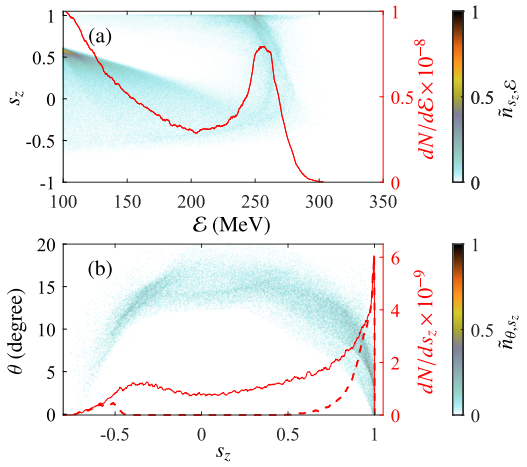

FIG. 9. (a) Density plot in $\mathscr{E}$–s_z space of protons from the three-dimensional simulation at $t = 500\tau$, together with the energy spectrum of all energetic protons (solid red curve). (b) Density plot in s_z–θ space of accelerated protons within the FWHM of the energy peak in (a). The solid red curve shows the corresponding longitudinal spin spectrum and the dashed red curve the spectrum of protons within the FWHM of the energy peak for $\theta < 10°$.

Following on from the above two-dimensional PIC simulations, to provide further understanding of the acceleration process and to verify the practical efficiency of the acceleration scheme, three-dimensional PIC simulations are conducted using the extended EPOCH code. The size of the simulation box is $180\lambda \times 24\lambda \times 24\lambda$, with cells of $1800 \times 240 \times 240$ and six pseudoparticles per cell for protons, electrons, and chlorine nuclei. The power of the driving laser power is increased to 7.7 PW, with a laser amplitude of $a_0 = 200$ and a pulse duration of 8τ. The plasma density and the length of the uniform plateau are set as $n_e = 0.72n_c$ and $z_2 - z_1 = 250\lambda$, respectively. The remaining parameters are identical to those used in the two-dimensional simulations for Fig. 7.

Figure 9(a) depicts the energy spectrum of the protons from the three-dimensional simulations at $t = 550\tau$, together with the corresponding density plot in $\mathscr{E}$–s_z space. An energy peak is observed at 257 MeV. It is notable that the protons at the energy peak have a relatively large s_z. The beam energy is significantly lower than that predicted by the two-dimensional simulations, owing to the magnetic vortex-induced acceleration field being reduced in the three-dimensional scenario, which could be attributable to the effect of dimension on laser-induced electron heating.[72] Nevertheless, protons are still accelerated to ~20 MeV by the laser-driven bubble according to Eqs. (5) and (6). Their energy is significantly boosted via MVA at the rear boundary of the target. Additionally, these polarized proton beams with energy $\gtrsim$200 MeV can be considered as an alternative injector for polarized colliders.[29–31]

Figure 9(b) presents a density plot in s_z–θ space of protons within the full width at half maximum (FWHM) of the energy peak, where $\theta = \tan^{-1}\left(\sqrt{p_x^2 + p_y^2}/p_z\right)$ is the spread angle. The corresponding longitudinal spin spectrum is shown by the solid red curve and indicates a beam polarization of 39.5%. The majority of protons are within a spread angle $\theta \lesssim 15°$. The density plot reveals that protons with smaller θ have higher s_z. If protons with $\theta < 10°$ are selected, then the beam polarization increases to 73.3%. The corresponding longitudinal spin spectrum of protons with $\theta < 10°$ is shown by the dashed red curve. The beam polarization increases further to 88.8% if only protons with $\theta < 5°$ are considered. Therefore, more stringent requirements for beam polarization can be met by using a smaller collection angle. The beam charge at the FWHM of the energy peak is 349 pC. This is reduced to 95.4 and 23.1 pC for collection angles of 10° and 5°, respectively.

VI. CONCLUSION

Laser-driven ion acceleration in a pre-polarized hydrogen halide gaseous target is expected to generate energetic spin-polarized protons economically. When a PW laser passes through a hydrogen halide gas jet, protons are accelerated by the laser-driven relativistic channel and wakefield inside the target, as well as by the stationary electric field at the rear boundary of the target. In particular, longitudinal motion of protons in the plasma wave triggers the injection of protons into the magnetic-vortex-enhanced acceleration field. In this study, the acceleration and spin precession of protons have been analyzed on the basis of the TBMT equation and analytical models of the laser-driven blowout bubble–channel structure. It has been found that the magnetic vortex affects the precession of protons in this structure and at the rear boundary of the target. By analyzing the proton dynamics and the field structures, the dependence of the final beam energy and polarization on laser and plasma parameters has been examined. It has been found that the energy gain is determined by the pre-acceleration of the protons in the plasma wave and the post-acceleration out of the target. Compared with our initial demonstration of energetic polarized proton beam generation,[38] the proton pre-acceleration within the plasma wave has been enhanced using our analytical model,[44,45] resulting in a significant increase in the final energy gain. Results from multidimensional PIC simulations indicate that monoenergetic proton beams with energies in the several hundred MeV range and a polarization of tens of percent can be achieved using PW-scale lasers and a pre-polarized gaseous target. This method can serve as an alternative to a polarized ion injection linac for use in a polarized collider.[28–31] Our study has thus provided a novel approach to high-energy laser-driven polarized proton acceleration, offering a practical proposal for polarized particle colliders.

ACKNOWLEDGMENTS

This work was supported by the National Natural Science Foundation of China (Grant Nos. 12075081 and 12404395) and the Innovation Group Project of the Natural Science Foundation of Hubei Province of China (Grant No. 2024AFA038). Bin Liu acknowledges the support of Guangdong High Level Innovation Research Institute Project, Grant No. 2021B0909050006.

AUTHOR DECLARATIONS

Conflict of Interest

The authors have no conflicts to disclose.

Author Contributions

Zhikun Zou: Data curation (equal); Software (equal). **Gan Guo**: Data curation (equal); Validation (equal). **Meng Wen**: Funding acquisition (equal); Supervision (equal); Writing – original draft (equal). **Bin Liu**: Formal analysis (equal); Funding acquisition (equal); Methodology (equal); Writing – review & editing (equal). **Xue Yan**: Formal analysis (equal); Resources (equal). **Yangjié Liu**: Conceptualization (equal); Writing – review & editing (equal). **Luling Jin**: Conceptualization (equal); Supervision (equal); Visualization (equal); Writing – review & editing (equal).

DATA AVAILABILITY

The data that support the findings of this study are available from the corresponding author upon reasonable request.

REFERENCES

[1]C. N. Danson, C. Haefner, J. Bromage, T. Butcher, J.-C. F. Chanteloup *et al.*, "Petawatt and exawatt class lasers worldwide," High Power Laser Sci Eng. **7**, e54 (2019).

[2]Z. Li, Y. Leng, and R. Li, "Further development of the short-pulse petawatt laser: Trends, technologies, and bottlenecks," Laser Photonics Rev. **17**, 2100705 (2022).

[3]W. Li, Z. Gan, L. Yu, C. Wang, Y. Liu *et al.*, "339 J high-energy Ti:sapphire chirped-pulse amplifier for 10 PW laser facility," Opt. Lett. **43**, 5681–5684 (2018).

[4]F. Lureau, G. Matras, O. Chalus, C. Derycke, T. Morbieu *et al.*, "High-energy hybrid femtosecond laser system demonstrating 2 × 10 PW capability," High Power Laser Sci. Eng. **8**, e43 (2020).

[5]G. A. Mourou, T. Tajima, and S. V. Bulanov, "Optics in the relativistic regime," Rev. Mod. Phys. **78**, 309–371 (2006).

[6]G. Mourou, "Nobel lecture: Extreme light physics and application," Rev. Mod. Phys. **91**, 030501 (2019).

[7]E. Esarey, C. B. Schroeder, and W. P. Leemans, "Physics of laser-driven plasma-based electron accelerators," Rev. Mod. Phys. **81**, 1229–1285 (2009).

[8]A. Macchi, M. Borghesi, and M. Passoni, "Ion acceleration by superintense laser–plasma interaction," Rev. Mod. Phys. **85**, 751–793 (2013).

[9]W.-J. Ma, Z.-P. Liu, P.-J. Wang, J.-R. Zhao, and X.-Q. Yan, "Experimental progress of laser-driven high-energy proton acceleration and new acceleration schemes," Acta Phys. Sin. **70**, 084102 (2021).

[10]F. Wagner, O. Deppert, C. Brabetz, P. Fiala, A. Kleinschmidt *et al.*, "Maximum proton energy above 85 MeV from the relativistic interaction of laser pulses with micrometer thick CH_2 targets," Phys. Rev. Lett. **116**, 205002 (2016).

[11]W. J. Ma, I. J. Kim, J. Q. Yu, I. W. Choi, P. K. Singh *et al.*, "Laser acceleration of highly energetic carbon ions using a double-layer target composed of slightly underdense plasma and ultrathin foil," Phys. Rev. Lett. **122**, 014803 (2019).

[12]I. J. Kim, K. H. Pae, I. W. Choi, C.-L. Lee, H. T. Kim *et al.*, "Radiation pressure acceleration of protons to 93 MeV with circularly polarized petawatt laser pulses," Phys. Plasmas **23**, 070701 (2016).

[13]W. P. Wang, C. Jiang, H. Dong, X. M. Lu, J. F. Li *et al.*, "Hollow plasma acceleration driven by a relativistic reflected hollow laser," Phys. Rev. Lett. **125**, 034801 (2020).

[14]T. Ziegler, I. Göthel, S. Assenbaum, C. Bernert, F.-E. Brack *et al.*, "Laser-driven high-energy proton beams from cascaded acceleration regimes," Nat. Phys. **20**, 1211 (2024).

[15]J. Bin, "Petawatt pulse pushes protons," Nat. Phys. **20**, 1055 (2024).

[16]F. Sylla, M. Veltcheva, S. Kahaly, A. Flacco, and V. Malka, "Development and characterization of very dense submillimetric gas jets for laser–plasma interaction," Rev. Sci. Instrum. **83**, 033507 (2012).

[17]I. Prencipe, J. Fuchs, S. Pascarelli, D. W. Schumacher, R. B. Stephens *et al.*, "Targets for high repetition rate laser facilities: Needs, challenges and perspectives," High Power Laser Sci. Eng. **5**, e17 (2017).

[18]V. Ospina-Bohórquez, C. Salgado-López, M. Ehret, S. Malko, M. Salvadori *et al.*, "Laser-driven ion and electron acceleration from near-critical density gas targets: Towards high-repetition rate operation in the 1 PW, sub-100 fs laser interaction regime," Phys. Rev. Res. **6**, 023268 (2024).

[19]B. Shen, Y. Li, M. Y. Yu, and J. Cary, "Bubble regime for ion acceleration in a laser-driven plasma," Phys. Rev. E **76**, 055402 (2007).

[20]X. Zhang, B. Shen, L. Zhang, J. Xu, X. Wang *et al.*, "Proton acceleration in underdense plasma by ultraintense Laguerre–Gaussian laser pulse," New J. Phys. **16**, 123051 (2014).

[21]C. A. J. Palmer, N. P. Dover, I. Pogorelsky, M. Babzien, G. I. Dudnikova *et al.*, "Monoenergetic proton beams accelerated by a radiation pressure driven shock," Phys. Rev. Lett. **106**, 014801 (2011).

[22]D. Haberberger, S. Tochitsky, F. Fiuza, C. Gong, R. A. Fonseca *et al.*, "Collisionless shocks in laser-produced plasma generate monoenergetic high-energy proton beams," Nat. Phys. **8**, 95–99 (2012).

[23]T. Nakamura, S. V. Bulanov, T. Z. Esirkepov, and M. Kando, "High-energy ions from near-critical density plasmas via magnetic vortex acceleration," Phys. Rev. Lett. **105**, 135002 (2010).

[24]J. Park, S. S. Bulanov, J. Bin, Q. Ji, S. Steinke *et al.*, "Ion acceleration in laser generated megatesla magnetic vortex," Phys. Plasmas **26**, 103108 (2019).

[25]I. Tazes, S. Passalidis, E. Kaselouris, D. Mancelli, C. Karvounis *et al.*, "Efficient magnetic vortex acceleration by femtosecond laser interaction with long living optically shaped gas targets in the near critical density plasma regime," Sci. Rep. **14**, 4945 (2024).

[26]T. Roser, L. Ahrens, J. Alessi, M. Bai, J. Beebe-Wang *et al.*, "First polarized proton collisions at RHIC," AIP Conf. Proc. **667**, 1–8 (2003).

[27]M. Burkardt, C. A. Miller, and W.-D. Nowak, "Spin-polarized high-energy scattering of charged leptons on nucleons," Rep. Prog. Phys. **73**, 016201 (2009).

[28]Y. Zhang, "JLEIC: A high luminosity polarized electron-ion collider at Jefferson lab," in *10th International Particle Accelerator Conference (IPAC2019)*, Melbourne, Australia, May 2019 (JACoW, 2019), paper TUPRB112, pp. 1916.10.18429/JACoW-NAPAC2019-TUPLO02.

[29]I. Alekseev, C. Allgower, M. Bai, Y. Batygin, L. Bozano *et al.*, "Polarized proton collider at RHIC," Nucl. Instrum. Methods Phys. Res., Sect. A **499**, 392–414 (2003).

[30]J. Martinez Marin, B. Mustapha, and L. Spentzouris, "Spin dynamics in the JLEIC ion injector linac," in *3rd North American Particle Accelerator Conference (NAPAC2019)*, Lansing, MI, Sep. 2019 (JACoW, 2019), paper TUPLO02, pp. 533.10.18429/JACoW-NAPAC2019-TUPLO02.

[31]B. Mustapha, Z. Conway, M. Kelly, A. Plastun, and P. Ostroumov, "Design of the multi-ion injector linac for the JLAB EIC (JLEIC)," J. Phys. Conf. **1401**, 012008 (2020).

[32]Y.-F. Li, R. Shaisultanov, K. Z. Hatsagortsyan, F. Wan, C. H. Keitel *et al.*, "Ultrarelativistic electron-beam polarization in single-shot interaction with an ultraintense laser pulse," Phys. Rev. Lett. **122**, 154801 (2019).

[33]A. S. Samsonov, E. N. Nerush, and I. Y. Kostyukov, "High-order corrections to the radiation-free dynamics of an electron in the strongly radiation-dominated regime," Matter Radiat. Extremes **8**, 014402 (2022).

[34]S. Tang, Y. Xin, M. Wen, M. A. Bake, and B. Xie, "Fully polarized Compton scattering in plane waves and its polarization transfer," Matter Radiat. Extremes **9**, 037204 (2024).

[35]M. Wen, M. Tamburini, and C. H. Keitel, "Polarized laser-wakefield-accelerated kiloampere electron beams," Phys. Rev. Lett. **122**, 214801 (2019).

[36]Z. Gong, M. J. Quin, S. Bohlen, C. H. Keitel, K. Põder *et al.*, "Spin-polarized electron beam generation in the colliding-pulse injection scheme," Matter Radiat. Extremes **8**, 064005 (2023).

[37]A. Hützen, J. Thomas, J. Böker, R. Engels, R. Gebel *et al.*, "Polarized proton beams from laser-induced plasmas," High Power Laser Sci. Eng. **7**, e16 (2019).

[38]L. Jin, M. Wen, X. Zhang, A. Hützen, J. Thomas *et al.*, "Spin-polarized proton beam generation from gas-jet targets by intense laser pulses," Phys. Rev. E **102**, 011201 (2020).

[39]D. Sofikitis, C. S. Kannis, G. K. Boulogiannis, and T. P. Rakitzis, "Ultrahigh-density spin-polarized H and D observed via magnetization quantum beats," Phys. Rev. Lett. **121**, 083001 (2018).

[40] A. K. Spiliotis, M. Xygkis, M. E. Koutrakis, K. Tazes, G. K. Boulogiannis *et al.*, "Ultrahigh-density spin-polarized hydrogen isotopes from the photodissociation of hydrogen halides: New applications for laser-ion acceleration, magnetometry, and polarized nuclear fusion," Light: Sci. Appl. **10**, 35 (2021).
[41] L. Reichwein, A. Pukhov, and M. Büscher, "Acceleration of spin-polarized proton beams via two parallel laser pulses," Phys. Rev. Accel. Beams **25**, 081001 (2022).
[42] X. Yan, Y. Wu, X. Geng, H. Zhang, B. Shen *et al.*, "Enhanced polarized proton acceleration driven by femtosecond laser pulses irradiating a micro-structured solid–gas target," Plasma Phys. Controlled Fusion **65**, 035005 (2023).
[43] X. F. Li, P. Gibbon, A. Hützen, M. Büscher, S. M. Weng *et al.*, "Polarized proton acceleration in ultraintense laser interaction with near-critical-density plasmas," Phys. Rev. E **104**, 015216 (2021).
[44] B. Liu, J. Meyer-ter-Vehn, K.-U. Bamberg, W. J. Ma, J. Liu *et al.*, "Ion wave breaking acceleration," Phys. Rev. Accel. Beams **19**, 073401 (2016).
[45] B. Liu, J. Meyer-ter-Vehn, and H. Ruhl, "Self-trapping and acceleration of ions in laser-driven relativistically transparent plasma," Phys. Plasmas **25**, 103117 (2018).
[46] J. W. Yoon, Y. G. Kim, I. W. Choi, J. H. Sung, H. W. Lee *et al.*, "Realization of laser intensity over 10^{23} W/cm^2," Optica **8**, 630–635 (2021).
[47] P. Wang, Z. Gong, S. G. Lee, Y. Shou, Y. Geng *et al.*, "Super-heavy ions acceleration driven by ultrashort laser pulses at ultrahigh intensity," Phys. Rev. X **11**, 021049 (2021).
[48] J.-R. Marquès, L. Lancia, P. Loiseau, P. Forestier-Colleoni, M. Tarisien *et al.*, "Collisionless shock acceleration of protons in a plasma slab produced in a gas jet by the collision of two laser-driven hydrodynamic shockwaves," Matter Radiat. Extremes **9**, 024001 (2023).
[49] O. Seemann, Y. Wan, S. Tata, E. Kroupp, and V. Malka, "Laser proton acceleration from a near-critical imploding gas target," Phys. Rev. Lett. **133**, 025001 (2024).
[50] B. Liu, B. Lei, Y. Gao, M. Wen, and K. Zhu, "Plasma opacity induced by laser-driven movement of background ions," Plasma Phys. Controlled Fusion **66**, 115004 (2024).
[51] A. B. Borisov, A. V. Borovskiy, V. V. Korobkin, A. M. Prokhorov, O. B. Shiryaev *et al.*, "Observation of relativistic and charge-displacement self-channeling of intense subpicosecond ultraviolet (248 nm) radiation in plasmas," Phys. Rev. Lett. **68**, 2309–2312 (1992).
[52] X. F. Shen, A. Pukhov, O. N. Rosmej, and N. E. Andreev, "Cross-filament stochastic acceleration of electrons in kilojoule picosecond laser interactions with near-critical-density plasmas," Phys. Rev. Appl. **18**, 064091 (2022).
[53] Y.-J. Gu and S. V. Bulanov, "Magnetic field annihilation and charged particle acceleration in ultra-relativistic laser plasmas," High Power Laser Sci. Eng. **9**, e2 (2021).
[54] A. Pukhov and J. Meyer-ter-Vehn, "Relativistic magnetic self-channeling of light in near-critical plasma: Three-dimensional particle-in-cell simulation," Phys. Rev. Lett. **76**, 3975–3978 (1996).
[55] T. D. Arber, K. Bennett, C. S. Brady, A. Lawrence-Douglas, M. G. Ramsay *et al.*, "Contemporary particle-in-cell approach to laser-plasma modelling," Plasma Phys. Controlled Fusion **57**, 113001 (2015).
[56] S. S. Bulanov, V. Y. Bychenkov, V. Chvykov, G. Kalinchenko, D. W. Litzenberg *et al.*, "Generation of GeV protons from 1 PW laser interaction with near critical density targets," Phys. Plasmas **17**, 043105 (2010).
[57] P. K. Singh, V. B. Pathak, J. H. Shin, I. W. Choi, K. Nakajima *et al.*, "Electrostatic shock acceleration of ions in near-critical-density plasma driven by a femtosecond petawatt laser," Sci. Rep. **10**, 18452 (2020).
[58] K. I. Popov, W. Rozmus, V. Y. Bychenkov, N. Naseri, C. E. Capjack *et al.*, "Ion response to relativistic electron bunches in the blowout regime of laser-plasma accelerators," Phys. Rev. Lett. **105**, 195002 (2010).
[59] L. L. Ji, A. Pukhov, I. Y. Kostyukov, B. F. Shen, and K. Akli, "Radiation-reaction trapping of electrons in extreme laser fields," Phys. Rev. Lett. **112**, 145003 (2014).
[60] B. Liu, J. Meyer-ter-Vehn, H. Ruhl, and M. Zepf, "Front edge velocity of ultraintense circularly polarized laser pulses in a relativistically transparent plasma," Plasma Phys. Controlled Fusion **62**, 085014 (2020).
[61] I. Göthel, C. Bernert, M. Bussmann, M. Garten, T. Miethlinger *et al.*, "Optimized laser ion acceleration at the relativistic critical density surface," Plasma Phys. Controlled Fusion **64**, 044010 (2022).
[62] B. Liu, M. Shi, M. Zepf, B. Lei, and D. Seipt, "Accelerating ions by crossing two ultraintense lasers in a near-critical relativistically transparent plasma," Phys. Rev. Lett. **129**, 274801 (2022).
[63] A. Pukhov, Z.-M. Sheng, and J. Meyer-ter-Vehn, "Particle acceleration in relativistic laser channels," Phys. Plasmas **6**, 2847–2854 (1999).
[64] T. W. Huang, C. T. Zhou, H. Zhang, S. Z. Wu, B. Qiao *et al.*, "Relativistic laser hosing instability suppression and electron acceleration in a preformed plasma channel," Phys. Rev. E **95**, 043207 (2017).
[65] S. Semushin and V. Malka, "High density gas jet nozzle design for laser target production," Rev. Sci. Instrum. **72**, 2961–2965 (2001).
[66] K. Schmid and L. Veisz, "Supersonic gas jets for laser-plasma experiments," Rev. Sci. Instrum. **83**, 053304 (2012).
[67] S. Lorenz, G. Grittani, E. Chacon-Golcher, C. M. Lazzarini, J. Limpouch *et al.*, "Characterization of supersonic and subsonic gas targets for laser wakefield electron acceleration experiments," Matter Radiat. Extremes **4**, 015401 (2019).
[68] I. Engin, Z. M. Chitgar, O. Deppert, L. D. Lucchio, R. Engels *et al.*, "Laser-induced acceleration of helium ions from unpolarized gas jets," Plasma Phys. Controlled Fusion **61**, 115012 (2019).
[69] O. Zhou, H.-E. Tsai, T. M. Ostermayr, L. Fan-Chiang, J. van Tilborg *et al.*, "Effect of nozzle curvature on supersonic gas jets used in laser–plasma acceleration," Phys. Plasmas **28**, 093107 (2021).
[70] Z.-Z. Lei, Y.-J. Gu, Z. Jin, S. Sato, A. Zhidkov *et al.*, "Supersonic gas jet stabilization in laser–plasma acceleration," High Power Laser Sci. Eng. **11**, e91 (2023).
[71] Z. Lécz, R. Polanek, A. Andreev, A. Sharma, D. Papp *et al.*, "Hybrid acceleration of compact ion bunches by few-cycle laser pulses in gas jets of two atomic species," Phys. Rev. Res. **5**, 023169 (2023).
[72] D. J. Stark, L. Yin, B. J. Albright, and F. Guo, "Effects of dimensionality on kinetic simulations of laser-ion acceleration in the transparency regime," Phys. Plasmas **24**, 053103 (2017).